NUMERICAL MODELING OF DYNAMIC CRACK PROPAGATION IN REINFORCED CONCRETE

R.C. Yu, X.X. Zhang and G. Ruiz
ETSI de Caminos, C.y P., Universidad de Castilla-La Mancha, 13071 Ciudad Real, Spain

RESUMEN

En este trabajo simulamos de modo explícito la propagación de fisuras en vigas de hormigón armado en régimen dinámico. Modelamos explícitamente la matriz de hormigón, las barras de armado y la intercara entre el acero y el hormigón. La nucleacin y propagación de fisuras en el hormigón en masa se representan gracias a un algoritmo de fragmentación que, al cumplirse las condiciones de apertura de grieta, inserta elementos cohesivos entre lo elementos de la malla original y, posteriormente, les deja ir abriéndose siguiendo un ablandamiento cohesivo. El tratamiento del deterioro del contacto acero-hormigón es semejante: en este caso se insertan elementos de intercara que permiten el deslizamiento relativo siguiendo leyes de adherencia. También se tratan explícitamente el contacto y la fricción en las nuevas superficies insertadas en la malla original. Estos elementos se integran en un código numérico que validamos frente a ensayos dinámicos de vigas de hormigón armado realizados en nuestro Laboratorio. Los resultados numéricos sugieren que la propagación se produce en dos etapas. En la primera la velocidad de propagación de la grieta es proporcional a la velocidad de carga. La segunda etapa consiste en una propagación inestable controlada básicamente por la energía mecánica almacenada en la viga.

ABSTRACT

In this work we simulate explicitly the dynamic fracture propagation in reinforced concrete beams. We represent the concrete matrix, the steel re-bars and the interface between the two materials explicitly. Therefore the crack nucleation within the concrete matrix, through and along the re-bars, the deterioration of the concrete-steel interface are modeled explicitly. The numerical simulations are validated against experiments of three-point-bend beams loaded dynamically under various strain rates. The numerical results suggest a two-stage crack propagation. The first stage corresponds to the stable crack advance, the second one, the unstable collapse of the beam.

KEY WORDS: Dynamic fracture, reinforced concrete.

1 INTRODUCTION

Many phenomenological models have been developed to study the problem of complex fracture processes in reinforced concrete specimens, in particular, when the propagation is static [1–4]. Those models focus on a crack that propagates through a reinforcement layer and that, at opening, causes the steel bars to be pulled-out. The main difficulty consists in modeling the propagation of the crack through the reinforcement layer, as such a layer— in 2D models— constitutes a discontinuity that stops the crack advance. Modeling the steel-concrete interaction is not simple either, since the pull-out process produces damage at the interface and it may also generate secondary fracture processes within the concrete bulk. Some of the aforementioned models solve both problems by substituting the rebars for closing forces applied at the crack lips; whose intensity relates to the strength of the reinforcement and of the interface [5, 6]. Some authors model the steel bars explicitly, however they only account for the extreme cases of perfect or null adherence [7]. Ruiz *et al.* [4] developed a simplified model that enables propagation of the crack through the reinforcement as well as interface deterioration. They adopted a computational strategy that consisted of overlapping both materials in the same spatial position. Concrete was modeled as a continuum, whereas steel was overlapped and connected by interface elements to nodes occupying the same initial position [8]. Concrete continuity allowed crack propagation through the reinforcement and interface elements transmitted shear stresses depending on the relative displacement between the two materials. However, their numerical model was not able to reproduce microcracking and/or damage around the main crack [3] and along the steel-concrete interface [9].

In dynamic regime, the fracture processes in reinforced concrete beams are more complicated than in the static case, as stress waves can be partly reflected from the steel-concrete interface and partly transmitted to the rebar. The interplay between the interface, steel re-bar and concrete matrix challenges the above numerical models, in which either the rebar is not physically represented [4–6], or the progressing deterioration of the interface is not reflected [7]. Indeed, such an interaction calls for an explicit modeling of those phenomena.

In this work, following previous efforts in explicitly modeling in static regime [10], we attempt to simulate explicitly the dynamic fracture propagation in reinforced concrete beams. In particular, adopting cohesive theories of fracture with the direct simulation of fracture and fragmentation [11, 12], we represent the concrete matrix, the steel re-bars and the interface between the two materials explicitly. Therefore the crack nucleation within the con-

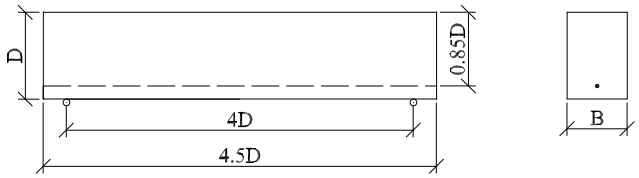

Figure 1: A reinforced concrete beam subjected to three point bending.

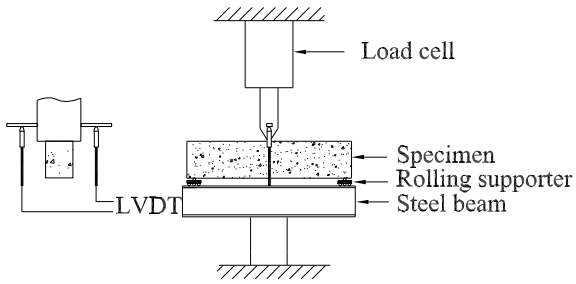

Figure 2: Experimental set-up for three-point bending tests on beams.

crete matrix, through and along the re-bars, the deterioration of the concrete-steel interface are modeled explicitly.

The organization of this paper is as follows. In the next section, the experimental setup is illustrated followed by the description of material characterization. A brief description of the cohesive model is provided in Section 4. In Section 5, the simulation results are discussed and finally, in Section 6, the work is summarized and some conclusions are drawn.

2 EXPERIMENTAL SETUP

Zhang et al. [13] conducted a series of tests in order to study the combined size and strain rate effect in lightly reinforced concrete beams. The loading rate ranged from 10^{-5} to 10^{-2}/s for beams of three sizes. The tests were carried out in a three-point-bend configuration as shown in Figure 1, where the width B is 50 mm, the depth D is 75 mm, 150 mm and 300 mm for small, medium and large specimens respectively. The specimens were casted to give a constant steel-reinforcement ratio of 0.15%. Figure 2 shows the experimental set-up for three-point bending tests. The specimen rests on two rigid-steel cylinders laid on two supports permitting rotation out of the plane of the beam and rolling along the beam longitudinal axis with negligible friction. These supports roll on the upper surface of a very stiff beam fastened to the machine actuator. The load-point displacement is measured in relation to points over the supports on the upper surface of the beam. Two LVDT (linear variable differential transducer) fixed on the steel beam are directly used to measure the displacement between the loading rod and the steel beam. For loading, a hydraulic servo-controlled test system was employed. The tests were performed in position-control. In numerical simulation, we take the experimental results of small specimens at a loading velocity of 7.5 mm/s for comparison. The strain rate at the bottom surface is related to this loading velocity through

$$V = \dot{\delta} = \dot{\epsilon} S^2 / 6D \tag{1}$$

where S and D are the span and depth of the beam, respectively, δ is the loading point displacement.

3 MATERIAL CHARACTERIZATION

A single micro-concrete was used throughout the experiment made with lime aggregates of 5 mm aggregate size and ASTM type II/A cement. The mix weight proportions were 3.2:0.5:1 for aggregate:water:cement conforming to ASTM C33. Table 1 shows the characteristic mechanical parameters of the micro-concrete determined in the various characterization and control tests, where f_c, f_t, E_c, G_F, ρ, are the compressive strength, tensile strength, elastic modulus, fracture energy, and mass density, respectively. The Hillerborg's characteristic length, calculated as $l_{ch} = E_c G_F / f_t^2$, is around 105 mm.

Table 1: *Micro-concrete mechanical properties*

	f_t MPa	f_c MPa	E_c GPa	G_F N/m	ρ kg/m^3
Mean	3.74	28.43	29.64	49.48	2113
Std. Dev	0.22	0.32	6.3	4.5.	-

The mechanical properties of the steel, the elastic moduli E_s, the standard yield strength $\sigma_{0.2}$, the ultimate strength σ_u and strain ϵ_u as well as the bond strength τ_c between the concrete and the rebar are all shown in Table 2.

4 NUMERICAL MODEL

We briefly summarize here the cohesive model adopted for the concrete matrix, further information can be found elsewhere and the references within [11, 14, 15]. A variety of mixed-mode cohesive laws accounting for tension-shear coupling [11, 16, 17], are established by the introduction of an effective opening displacement δ,

$$\delta = \sqrt{\beta^2 \delta_s^2 + \delta_n^2}, \tag{2}$$

which assigns different weights to the normal δ_n and sliding δ_s opening displacements. Supposing that the cohesive free-energy density depends on the opening displacements only through the effective opening displacement δ, a reduced cohesive law, which relates δ to an effective cohesive traction

$$t = \sqrt{\beta^{-2} t_s^2 + t_n^2}, \tag{3}$$

Table 2: *Mechanical properties of the steel re-bar and the interface bond strength*

E_s GPa	$\sigma_{0.2}$ MPa	σ_u MPa	ϵ_u -	τ_c MPa
133.2	434.1	465.1	0.9%	5.34 ± 0.80

where t_s and t_n are the shear and the normal tractions respectively, can be obtained [11,16]. The weighting coefficient β is considered a material parameter that measures the relation between the shear and tensile resistance of the material. The existence of a loading envelope defining a connection between t and δ under the conditions of monotonic loading, and irreversible unloading is assumed. A linear decreasing cohesive law is adopted in the calculations.

A damage variable d, is defined as the fraction of the expended fracture energy over the total fracture energy per unit surface. Thus, a damage value of zero denotes an uncracked surface, whereas a damage value of one is indicative of a fully cracked or free surface.

The cohesive model introduces an intrinsic time described by

$$t_c = \frac{\rho c \delta_c}{2 f_t} \tag{4}$$

where ρ represents the mass density, c, the longitudinal wave velocity, δ_c, the critical opening displacement. As shown in [15, 18], due to this intrinsic time, the cohesive model is able to respond differently for a slow and fast loading process. For the material properties given in Table 1, this value is calculated as 28 μs.

In treating the steel-concrete interface, we follow the methodology illustrated in Yu and Ruiz [10]. A cohesive-like interface element is implemented. This interface element is inserted only when the slip strength is attained. The sliding between two surfaces is governed by a perfect-plastic bond-slip law. The steel re-bar is modeled as an elastic-perfectly plastic material.

5 NUMERICAL RESULTS

We chose to model the small beam, 75 mm in depth to compare with the experimental results. The initial mesh consists of 6764 quadratic tetrahedrons and 10142 nodes. The mesh size near the middle surface, 7 mm, is chosen to be comparable to the maximum aggregate size, 5 mm, based on the convergence analysis done by Ruiz *et al.* [14, 15] in modeling plain concrete in a dynamic regime. The average mesh size that resolves the interface –around 10 mm– is designed to resolve the effective slip length L_s, which can be described as

$$L_s = A_s f_y / \tau_c p \tag{5}$$

according to Ruiz [3], where f_y is the yield strength, A_s is the steel cross-section area, p the rebar perimeter, τ_c the interface bond strength. L_s is computed as 54.3 mm.

We load the beam through an elastic spring to reflect the fact that in the experiments the load transfer is realized through a mechanical system (loading rod, reaction frame, etc.), whose stiffness is 38 kN/mm.

5.1 *Peak load*

The first step of the simulations was to check the predicted peak load. As we mentioned before, we expected the cohesive model to respond the dynamic loading. As the strain rate increases, the predicted peak loads should increase accordingly. But as can be seen from Figure 3, when the loading velocity is increased from 7.5 mm/s to 30 mm/s, the peak load is practically the same, while when we prescribed a loading velocity of 3000 mm/s (corresponds to a loading rate of 15 /s), the peak load increased from 4 kN to 10 kN. Even though we do not have

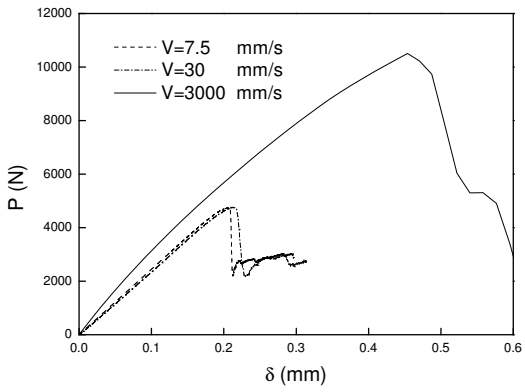

Figure 3: The load-displacement curves for loading velocity at 7.5, 30 and 3000 mm/s respectively, when static fracture properties (specific fracture energy and tensile strength) are adopted.

the experimental data for loading velocity of 3000 mm/s for comparison, the qualitative increase of the peak load has been captured. This shows that when the crack propagation time (7000 to 3000 μs) is not comparable to the intrinsic time of the cohesive model (28 μs), the strength increase cannot be captured. This also confirms the observations of Rossi and Toulemonde [19], who pointed out that: (a) at strain rates smaller than approximately 1/s, the moisture content is believed to play an important role in the strength increase of concrete, the free water in the micro-pores exhibits the so-called Stefan effect causing a strengthening in concrete with increasing loading rate. The main physical mechanism counters both a micro-cracking localization, leading to increase of concrete tensile strength, and the macro propagation that leads to failure of the specimen; (b) at strain rates higher than or equal to 10 /s, the micro-inertia effects in the fracture process zone might cause the rate dependence of concrete, whereas the moisture content is assumed not to be dominant. The main mechanism counters micro-cracking localization and in particular macro crack propagation. In order to capture the strength increase due to moisture content, which is not covered by the bulk constitutive law, we fit for the experimental data of Harsh *et al.* [20] to obtain a 30% increase for the fracture energy and the tensile strength. This gives us a peak load of 4.8 kN, comparable to the experimental data, which is shown in Figure 6. Note that we didn't tailor the material parameter to make the numerical simulation to fit the experiments, but followed an independent source that gives the rate-dependent material properties.

5.2 *Initial stiffness*

We observe in Figure 4 that there is a difference in the initial stiffness between the two experimental curves, this has been explained by Guinea, Planas and Elices [21], who pointed out that even in the case of identical beams made of the same material, the initial slopes may show variations. This is due to the sensitivity of the elastic flexibility of the beam to the boundary conditions in the ap-

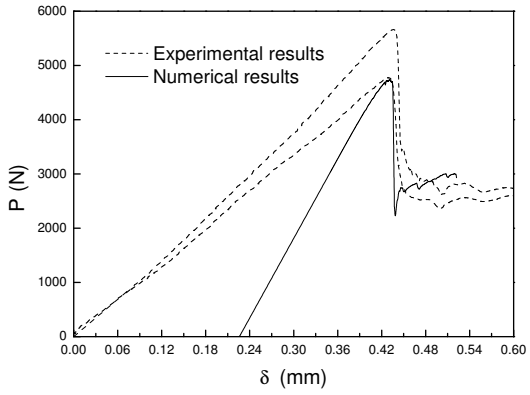

Figure 4: The numerical and experimental load-displacement comparison, when dynamic material properties (fracture energy and tensile strength) are adopted, note that the numerical curve has been translated to 0.24 mm for easier visualization of the peak load.

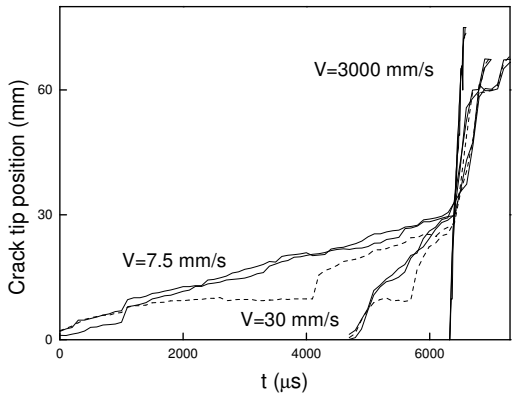

Figure 5: The crack tip position versus time for loading velocity at 7.5, 30 and 3000 mm/s respectively, where the solid lines corresponding to values measured at specimen surface, dotted lines represent values measured at specimen center.

plication of the concentrated load. Having in mind that, on the one hand, we would not know the exact experimental boundary condition but only the average, on the other hand the numerical discretization also introduces a pre-defined stiffness, this would all contribute to the deviation of the initial stiffness of the P-δ curve. But we want to emphasize that the post-peak behavior, for both the two experimental data and the numerical simulation, shows similarity. This gives us confidence for the succeeding analysis in extracting the crack tip velocities and the CMOD history.

5.3 *Crack tip velocities*

The crack tip positions for three different loading velocities, 7.5 mm/s, 30 mm/s and 3000 mm/s are plotted against time in Figure 5. The crack tip positions at the central cross section of the beam were measured separately at the two vertical edges (solid line) and at the center (dashed line) from the bottom of the specimen. The crack tip position is measured with respect to the damage variable value of 0.05 in all the cases. In addition, the axes of the graphs in the proceeding figures have been adjusted to make the comparison easier. For loading velocities 7.5 mm/s and 30 mm/s, the crack velocities at the edges are approximately the same, showing a symmetric crack propagation with respect to the central line. The crack tip position at the center exhibits a plateau due to the hindrance of the steel rebar. The initial slopes of the curves show a linear dependence on the loading velocity. For example, as shown in Table 3, the initial slopes for 7.5 and 30 mm/s are 3.5 m/s and 14.8 m/s respectively. A change in slope is observed at the peak load after which the new slope shows a marked similarity in both the cases. For loading velocity 3000 mm/s, the slope of the curve is steep since the loading velocity is faster and the run completes in a shorter time span. In short, it is evident that crack tip velocity is close after the peak load is reached and it does not depend very much on the loading velocity. The second slope for loading velocity of 7.5 mm/s is about 20 times larger than its first slope, while for 30 mm/s is about 10 times larger. We can say that the crack went through a stable-to-unstable transition when the loading velocity is relatively low. However, at higher loading rate, the whole process is unstable.

In addition, in Figure 6 we plot the load history around the peak load, against the crack tip position history for loading velocity of 7.5 mm/s. It shows that the main crack initiated around 80% (3800 N) of the maximum load (4800 N), and the attainment of the peak load marks the turning point of the two-stage crack propagation.

5.4 *CMOD history*

The crack mouth opening displacements for loading velocities, v = 7.5, 30, 3000 mm/s were obtained numer-

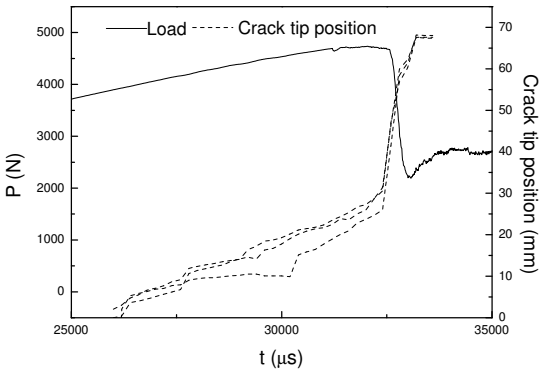

Figure 6: The zoomed view of the load history plotted against the crack tip position history for loading velocity of 7.5 mm/s.

Table 3: *Crack tip velocity (m/s)*

	Loading velocity (mm/s)		
	7.5	30	3000
	At surfaces		
Pre-peak	3.9	15.6	290
Post-peak	70.5	95.4	280.5
	At center		
Pre-peak	3.5	14.8	296
Post-peak	75.7	112.4	289

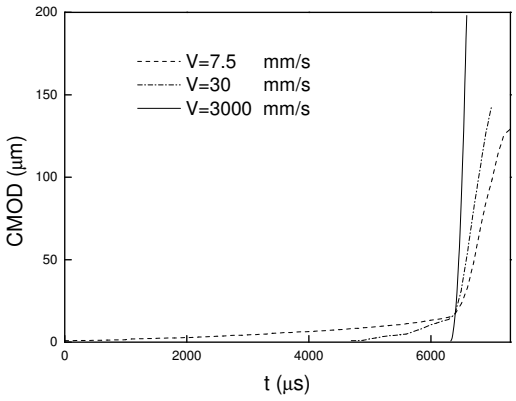

Figure 7: The CMOD history at 7.5, 30 and 3000 mm/s respectively.

ically at the central line of the bottom surface of the beam. The CMOD curves for aforementioned velocities are plotted in Figure 7. The curves exhibit a similar trend for all the loading velocities. They consist of two sections with different and approximately linear slopes; let us call them as the first and the second slope, the turning point marks the time of reaching peak load. The detailed information is shown in Table 4. For loading velocity v=7.5 and 30 mm/s, the first slope changes by approximately the same factor by which the velocities are scaled; after the peak load, the CMOD rate is suddenly increased by around two orders of magnitude compared with that before peak load. This also means that the crack propagation shows a transition from stable to unstable state. While for loading velocity v=3000 mm/s, the CMOD rate before the peak load and after the peak load is similar, the whole crack propagation is unstable. As seen earlier, this trend is similar as compared to the crack tip position curves (Figure 5).

5.5 *Crack patterns*

We paid close attention to the crack patterns of the reinforced beams at three characteristic point of the loading process: the intermediate time between the time of crack initiation and the time of reaching the peak load, the time of reaching the peak load and the time of breaking the beam. These patterns are illustrated from the loading plane (middle surface), as shown in Figure 8. It shows that the crack patterns are similar for the two smaller loading velocities, whereas for 3000 mm/s, the crack is noticeably more advanced.

Table 4: CMOD rate (m/s)

	Loading velocity (mm/s)		
	7.5	30	3000
Pre-peak	0.002	0.0094	0.17
Post-peak	0.13	0.242	1.26

6 CONCLUSIONS

We have compared the numerical load-displacement curves to the experimental counterparts for three-point-bend beams lightly reinforced with steel re-bars. We have extracted numerically the crack tip velocity and CMOD history. The results suggest a two-stage crack propagation. The first stage corresponds to the stable crack advance, the second one, the unstable collapse of the beam. Both the crack tip velocities and the CMOD rate have a linear dependence depending upon the factor by which the loading velocity is scaled for the first slopes. The second slope does not depend on the loading velocity and hence it exhibits similar slopes for all loading velocities. The crack patterns advancing at different stages are also analyzed.

7 ACKNOWLEDGMENTS

We would like to acknowledge the financial support from the *Dirección General de Investigación*, Spain, through Grant MAT2006-09105. Rena C. Yu thanks the *DGI*, Spain, for the funding from the *Programa Ramón y Cajal*.

References

[1] C. Bosco and A. Carpinteri. Fracture behaviour of beam cracked across reinforcement. *Theoretical and Applied Fracture Mechanics*, 17:61–68, 1992.

[2] G. Ruiz, M. Elices, and J. Planas. *Size Effect and Bond-Slip Dependence of Lightly Reinforced Concrete Beams*, pages 67–98. Elsevier, ESIS Publication 24, Kidlington, Oxford, UK, 1999.

[3] G. Ruiz. Propagation of a cohesive crack crossing a reinforcement layer. *International Journal of Fracture*, 111:265–282, 2001.

[4] G. Ruiz, J. R. Carmona, and D. A. Cedón. Local fracture and steel-concrete decohesion phenomena studied by means of cohesive interface elements. *Computer Methods in Applied Mechanics and Engineering*, page in press, 2006.

[5] O. Hededal and I. B. Kroon. *Lightly reinforced high-strength concrete, M. Sc. Thesis*. University of Åalborg, Denmark, 1991.

[6] R. Brincker, M. S. Henriksen, F. A. Christensen, and G. Heshe. *Size effects on the bending behaviour of reinforced concrete beams.*, pages 127–180. Elsevier, London, 1999.

[7] N. M. Hawkins and K. Hjorsetet. *Minimum reinforcement requirement for concrete flexural members.*, pages 379–412. Elsevier, London, 1992.

[8] N. M. Hawkins and K. Hjorsetet. *Bond of RC members using nonlinear 3D FE analysis*, pages 861–868. IA-FraMCoS, 2004.

[9] M. R. Ben Romdhane and D. R. Ulm. Computational mechanics of the steel-concrete interface. *International Journal for Numerical and Analytical Methods in Geomechanics*, 26:99–120, 2002.

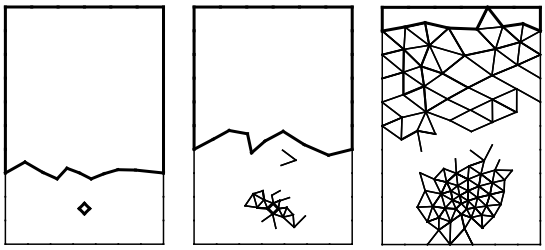

(a)

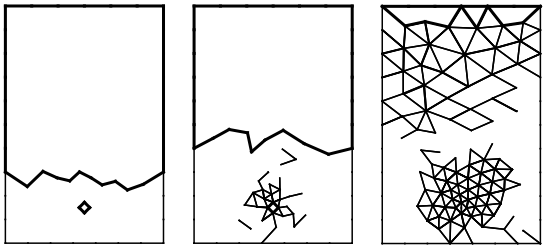

(b)

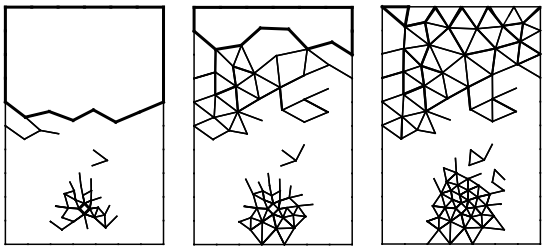

(c)

Figure 8: The main crack front advancing (the thick line within the frame) and micro crack formation (the thin lines which coincide with the element boundaries) for loading velocity of 7.5, 30, and 3000 mm/s.

[10] R. C. Yu and G. Ruiz. Explicit Finite Element Modeling of Static Crack Propagation in Reinforc ed Concrete. *International Journal of Fracture*, page in press, 2006.

[11] M. Ortiz and A. Pandolfi. Finite-deformation irreversible cohesive elements for three-dimensional crack-propagation analysis. *International Journal for Numerical Methods in Engineering*, 44:1267–1282, 1999.

[12] A. Pandolfi and M. Ortiz. An Efficient Adaptive Procedure for Three-Dimensional Fragmentation Simulations. *Engineering with Computers*, 18(2):148–159, 2002.

[13] X. X. Zhang, G. Ruiz, and R. C. Yu. Combined strain rate and size effect in reinforced concrete, an experimental study. *Engineering Fracture Mechanics*, page submitted, 2006.

[14] G. Ruiz, M. Ortiz, and A. Pandolfi. Three-dimensional finite-element simulation of the dynamic Brazilian tests on concrete cylinders. *International Journal for Numerical Methods in Engineering*, 48:963–994, 2000.

[15] G. Ruiz, A. Pandolfi, and M. Ortiz. Three-dimensional cohesive modeling of dynamic mixed-mode fracture. *International Journal for Numerical Methods in Engineering*, 52:97–120, 2001.

[16] G. T. Camacho and M. Ortiz. Computational modelling of impact damage in brittle materials. *International Journal of Solids and Structures*, 33 (20-22):2899–2938, 1996.

[17] A. De Andres, J. L. Perez, and M. Ortiz. Elastoplastic finite-element analysis of three-dimensional fatigue crack growth in aluminum shafts subjected to axial loading. *International Journal of Solids and Structures*, 36(15):2231–2258, 1999.

[18] R. C. Yu, G. Ruiz, and A. Pandolfi. Numerical investigation on the dynamic behavior of advanced ceramics. *Engineering Fracture Mechanics*, 71:897–911, 2004.

[19] P. Rossi and E. Toulemonde. Effect of loading rate on the tensile behavior of concrete:description of the physical mechanisms. *Materials and Structures*, 29(186):116–118, Mar 1996.

[20] S. Harsh, Z. J. Shen, and D. Darwin. Strain-rate sensitive behavior of cement paste and mortar in compression. *ACI Materials Journal*, 87(6):508–516, Sep-Oct 1990.

[21] J. Planas, G. Guinea, and M. Elices. Stiffness associated with quasi-concentrated load. *Materials and Structures*, 27:311–318, 1992.